Adsorption of tricresyl phosphate onto graphene nanomaterials from aqueous solution

Jun Liu, Siying Xia, Xiaomeng Lü and Hongxiang Shen

ABSTRACT

Phosphorus flame retardant tricresyl phosphate (TCP) adsorption on graphene nanomaterials from aqueous solutions was explored using batch and column modes. Comparative studies were performed regarding the kinetics and equilibrium of TCP adsorption on graphene oxide (GO) and graphene (G) in batch mode. The adsorption kinetics exhibited a rapid TCP uptake, and experimental data were well described by the pseudo-second-order kinetic model. Adsorption isotherm data of TCP on the two adsorbents displayed an improved TCP removal performance with increasing temperature at pH 5, while experimental data were well described by the Langmuir isotherm model with a maximum adsorption capacity of 87.7 $mg \cdot g^{-1}$ for G, and 30.7 $mg \cdot g^{-1}$ for GO) at 303 K. The thermodynamic parameters show that the adsorption reaction is a spontaneous and endothermic process. In addition, dynamic adsorption of TCP in a fixed G column confirmed a faster approach to breakthrough at high flow rate, high influent TCP concentration, and low filling height of adsorbent. Breakthrough data were successfully described by the Thomas and Yoon-Nelson models.

Key words | batch and column modes, breakthrough, isotherm, phosphorus flame retardants, physico-chemical treatment

Jun Liu (corresponding author)
Siying Xia
School of the Environment and Safety Engineering,
Jiangsu University,
Zhenjiang 212013,
China
E-mail: *liujun1227@ujs.edu.cn*

Xiaomeng Lü
School of Chemistry and Chemical Engineering,
Jiangsu University,
Zhenjiang 212013,
China

Hongxiang Shen
Shanghai Aerospace Control Technology Institute,
Shanghai 200233,
China

INTRODUCTION

With the gradual phase-out of some brominated flame retardants (BFRs) due to their persistency and toxicity, phosphorus flame retardants (PFRs), which have already been used worldwide for several decades, are often considered as suitable substitutes for BFRs. Due to their extensive use, PFRs have been reported in drinking water (Ding *et al.* 2015), surface water (Martínez-Carballo *et al.* 2007), groundwater (Regnery *et al.* 2011), air (Ren *et al.* 2016), dust (Cao *et al.* 2014a; He *et al.* 2015), sediments (Cao *et al.* 2014b), soil (Lu *et al.* 2014), fishes (Kim *et al.* 2011), and even human samples (Ding *et al.* 2015).

Recently, risk assessments have recognized that some PFRs, such as tris (chloroethyl) phosphate and tris (2,3-dichloropropyl) phosphate, tri-*n*-butyl phosphate, triphenyl phosphate, and tricresyl phosphate (TCP) are carcinogenic, mutagenic, or neurotoxic (van der Veen *et al.* 2012; Wei *et al.* 2015). These results indicate that PFRs have a large impact on the environment, and are potentially toxic to humans. Therefore, it is important to remove PFRs from the environment. A few studies have focused on the efficient elimination of PFRs from aqueous solutions by oxidation (Ishikawa *et al.* 1992; Yuan *et al.* 2015), but other traditional techniques such as photocatalytic degradation, membranes, and adsorption are not still used to remove PFRs from polluted water. Among these methods, adsorption techniques are used widely for water and wastewater pretreatment because they are simple and effective. Additionally, graphene exhibits superior adsorption capabilities for different pollutants in recent years due to its unique physico-chemical properties (Zhao *et al.* 2011b; Xu *et al.* 2012; Al-Khateeb *et al.* 2014; Wang *et al.* 2014; Jin *et al.* 2015; Liu *et al.* 2015a, 2015b; Zhou *et al.* 2015). To our knowledge, however, no studies have been conducted to investigate the adsorption of PFRs onto graphene.

In this study, graphene was used for the first time to adsorb a most frequently used PFR, TCP, from aqueous solutions. First, the adsorption kinetics, equilibrium, and thermodynamics were investigated in batch mode. In addition, the effects of contact time, initial concentration, pH and temperature on the adsorption of TCP were also evaluated. Furthermore, dynamic adsorption was performed, and the influences of flow rate, graphene mass,

doi: 10.2166/wst.2017.317

and inlet concentration were also investigated, which could offer new insights for the better design of graphene-based adsorbents or other wastewater pretreatment applications.

EXPERIMENTAL SECTION

Materials

Graphite powders were purchased from Alfa Aesar. TCP ($C_{21}H_{21}O_4P$) and all other chemicals were purchased from Sinopharm Chemical Reagent Co., Ltd. Graphene oxide (GO) and graphene were synthesized according to the former method (Liu *et al.* 2015a, 2015b) and the detailed preparation and characterization methods are described in the Supplemental Material (available with the online version of this paper).

Preparation of GO and graphene

GO was synthesized from natural graphite flake using a modified Hummers method (Marcano *et al.* 2010; Xu *et al.* 2012; Liu *et al.* 2015a, 2015b). Concentrated H_2SO_4 (360 mL), H_3PO_4 (40 mL) and $KMnO_4$ (18.0 g) were added to graphite flakes (3.0 g). The resulting mixture was heated to 50 °C and stirred for 12 h then it was poured into deionized water (1,000 mL) and 30% H_2O_2 (10 mL). The mixture was centrifuged (8,000 rpm) for 1 h, and the supernatant was decanted away. Then the remaining solid material was washed with 30% HCl and water three times, respectively. For each wash, the mixture was centrifuged (8,000 rpm) for 1 h and the supernatant decanted away. The obtained solid material after several wash processes was dried in a vacuum at 40 °C for 6 h.

Graphene was synthesized by the hydrazine reduction of GO (Xu *et al.* 2012). 500 mg GO was added to 250 mL of deionized water, and the mixture was ultrasonicated for 2 h. Moderate ammonia solution was added to regulate the pH to 10, then 5 mL of hydrazine hydrate (75%) was added to the solution at 95 °C and the system was stirred for 5 h. The black solution was filtered, washed thoroughly with deionized water to remove the excess hydrazine, and finally dried at room temperature.

Characterization

The crystalline structures analysis was carried out on an X-ray diffraction (XRD) instrument (D8 ADVANCE, BRUKER). Fourier transformed infrared (FTIR) spectra were recorded on a Nicolet Nexus 470 (Thermo Nicolet) with a resolution in transmission mode at room temperature. The Raman spectra and specific surface areas were obtained by DXR Raman spectroscopy and Brunauer–Emmett–Teller (BET), respectively.

Batch adsorption experiments

Adsorption studies were carried out by batch adsorption experiments in a conical flask at different conditions. A stock solution of 1,000 mg L^{-1} of TCP was prepared with a mixed solution of deionized water-methyl alcohol (1:1, v/v) because of its low solubility in water and was further diluted with the mixed solution to the required concentrations before use. After being shaken for 6 h (TDL-4, Shanghai Anting Scientific Instrument Factory, Shanghai, China), which was enough for TCP to achieve adsorption equilibrium according to preliminary experiments, the suspensions were filtered through 0.45 μm membrane filters for the concentration of TCP analysis using high performance liquid chromatography (HPLC, LC-10AT, SHIMADZU). The initial pH of the solution was adjusted by addition of 0.1 M HCl or NaOH solution.

The amount of TCP adsorbed on the adsorbents at equilibrium, q_e (mg·g^{-1}), was calculated using the equation

$$q_e = V \times \frac{C_0 - C_e}{m} \quad (1)$$

where C_0 and C_e are the initial and equilibrium concentrations of TCP in solution (mg·L^{-1}), respectively; V is the volume of the solution (mL), and m is the weight of the adsorbent (mg).

Kinetic experiments

In adsorption kinetic studies, the initial pH of the solution (100 mL) was adjusted to 5 by the addition of 0.1 M HCl. The initial concentration of TCP was 5 mg·L^{-1}. Then, 10 mg of the adsorbent was added at 303 K. The flasks were sealed and shaken at 200 rpm for 6 h using a thermostatic water bath shaker (TDL-4, Shanghai Anting Scientific Instrument Factory, Shanghai, China). Two mL was withdrawn from the bulk solution at certain time intervals and filtered immediately with 0.45 μm membrane filters for HPLC analysis. The pseudo-first-order rate equation is widely used for description of kinetic data and is presented in linear form as follows:

$$\ln(q_e - q_t) = lnq_e - k_1 t \quad (2)$$

where q_e and q_t are the amount of TCP adsorbed on the adsorbent at equilibrium and at various times t (mg·g^{-1}),

respectively, and k_1 is the rate constant of the pseudo-first-order model of adsorption (min^{-1}).

The pseudo-second-order model is expressed by the following equation (Ho & McKay 1998):

$$\frac{t}{q_t} = \frac{1}{k_2 q_e^2} + \frac{t}{q_e} \tag{3}$$

where q_e and q_t are defined as in the pseudo-first-order model and k_2 is the rate constant of the pseudo-second-order model of adsorption ($g \cdot mg^{-1} \cdot min^{-1}$). The intraparticle diffusion model is presented as

$$q_t = k_i t^{1/2} + C \tag{4}$$

where C is the intercept and k_i is the intraparticle diffusion rate constant ($mg \cdot g^{-1} \cdot min^{-1/2}$).

Equilibrium experiments

In adsorption isotherm studies, 10 mg of G were brought into contact with TCP solution and shaken for 6 h at 303 K, 323 K and 343 K, respectively. The pH of the TCP solution was adjusted to 5, and the initial concentration of TCP varied from 5 to 50 $mg \cdot L^{-1}$. The solutions in equilibrium were sampled and filtered for HPLC analysis. The Langmuir and Freundlich equations in linear form are as follows.

Langmuir model:

$$\frac{C_e}{q_e} = \frac{C_e}{q_m} + \frac{1}{q_m K_L} \tag{5}$$

Freundlich model:

$$\ln q_e = \frac{1}{n} \ln C_e + \ln K_F \tag{6}$$

where C_e is the equilibrium concentration of TCP in solution ($mg \cdot L^{-1}$), q_e is the adsorption capacity at equilibrium ($mg \cdot g^{-1}$), q_m is the maximum amount of TCP absorbed on the adsorbent ($mg \cdot g^{-1}$), K_L is the equilibrium adsorption constant ($L \cdot mg^{-1}$), and K_F ($mg \cdot g^{-1} \cdot L^{-1/n} \cdot mg^{-1/n}$) and n are Freundlich constants related to the adsorption capacity and adsorption intensity, respectively.

Calculation of thermodynamic parameters

To further explore the information about internal energy changes that are associated with adsorption, the standard free-energy change (ΔG°), the standard enthalpy change (ΔH°), and the standard entropy change (ΔS°) are calculated from the temperature-dependent adsorption isotherms to predict the adsorption process. The standard free energy change (ΔG°) can be calculated from the following equation:

$$\Delta G^o = -RT \ln K^o \tag{7}$$

where K^o ($L \cdot g^{-1}$) is the adsorption equilibrium constant, R is the universal gas constant (8.314 $J \cdot mol^{-1} \cdot K^{-1}$) and T is the absolute temperature (K). The values of $\ln K^o$ are obtained by plotting $\ln K_d$ versus C_e and extrapolating C_e to zero (K_d is the distribution adsorption coefficient). These intercepts at the vertical axis provide the value of $\ln K^o$. K_d is calculated from the following equation (Liu *et al.* 2015a; Zhao *et al.* 2011a):

$$K_d = \frac{q_e}{C_e} \tag{8}$$

The standard enthalpy change (ΔH°) and the standard entropy change (ΔS°) can be calculated using the following equation (Liu *et al.* 2015a; Zhao *et al.* 2011a):

$$\ln K^o = \frac{\Delta S^o}{R} - \frac{\Delta H^o}{RT} \tag{9}$$

The values of ΔH° and ΔS° were determined from the slope and the intercept of the plots of $\ln K^o$ versus $1/T$, respectively.

Column adsorption tests

Continuous column adsorption studies were performed at 298 K using a U-tube to evaluate the performance of graphene for TCP removal from aqueous solutions. The column was packed with different masses of graphene (0.9 g, 1.8 g, or 2.7 g). In order to obtain uniform flow distribution and to avoid the loss of graphene, quartz sand was packed inside the U-tube as shown in Figure 1. The initial concentration and pH of the TCP feed solution was 1 $mg \cdot L^{-1}$ and 5, respectively. The TCP solution was continuously pumped to the column at a flow rate of 3 $mL \cdot min^{-1}$ using a peristaltic pump. The effluent samples were collected at predetermined time intervals using a fraction collector and were analyzed by HPLC for TCP concentration.

HPLC analysis

TCP concentrations were determined by HPLC (SHIMADZU LC-10AT) fitted with a C18 column (250 mm × 4.6 mm) at

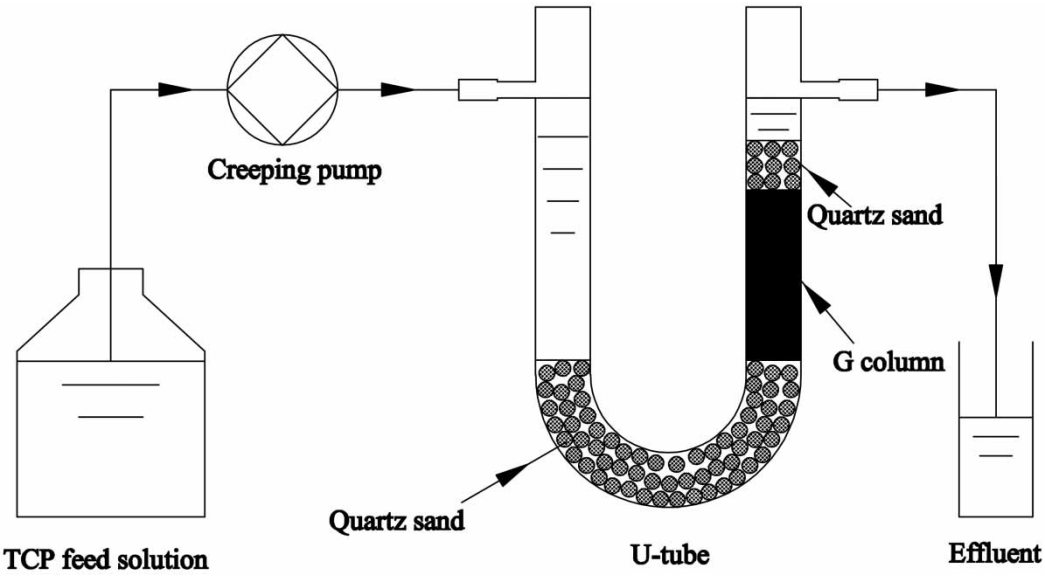

Figure 1 | Experimental setup of dynamic adsorption.

the absorption maximum wavelength of 264 nm. Isocratic elution was performed at a flow rate of 1 mL·min^{-1} and the mobile phase was methanol. The injection volume was 10 μL. All samples were filtered through membrane filters of 0.45 μm prior to analysis.

RESULTS AND DISCUSSION

Characterization

The results of XRD, Raman, and FTIR characterization of graphite, GO and graphene (G) are shown in Figure S1 (available with the online version of this paper). In the XRD patterns (Figure S1(a)), the peak at $2\theta = 10.03^{\circ}$ corresponds to the typical (001) diffraction peak of GO nanosheets, which demonstrated the loose-layer-like structure of GO with interlayer spacing of about 0.80 nm. However, the peak vanished in the pattern of G, and a weak (002) diffraction peak showed at about 26.5°, corresponding to the structure of G with interlayer spacing of about 0.37 nm. This was because the oxygen-containing groups between carbon layers were nearly removed by hydrazine hydrate. The Raman spectra of GO and G show the prominent D peak (1,350 cm^{-1}) and G peak (1,580 cm^{-1}), while the intensity ratio of D band to G band (I_D/I_G) of GO increases from 0.96 to 1.20 after hydrazine hydrate reduction (Figure S1(b)). This indicates a decrease in the average size of the sp^2 domain in G, which means that G is more disordered than GO. Different functional groups are found in the FTIR spectrum of GO (Figure S1(c)); that is, –COOH at 3,000 cm^{-1}, –COH at 3,400 cm^{-1}, C–O group at 1,220 cm^{-1}, and C=O group at 1,730 cm^{-1}, which all disappeared in the spectrum of G, indicating the efficient reduction of hydroxyl and carboxyl groups. All these characterization results confirm that GO and G have been prepared successfully.

Adsorption kinetics

The adsorption kinetics of TCP to GO and G are displayed in Figure 2. For GO and G, the adsorption equilibrium can be reached in less than 6 h. G has a higher adsorption rate than GO, which may be attributed to the higher specific surface areas of G (Table S1, available online). In order to illustrate the adsorption kinetics process, the pseudo-first-order, pseudo-second-order and intraparticle diffusion models were employed to fit experimental data. Results are shown in Figure 2 and Figure S2 (available online), and fitting parameters are listed in Table 1. For GO and G, the correlation coefficients (R^2) for the pseudo-second-order were relatively higher than those of the pseudo-first-order model, indicating that the pseudo-second-order kinetic model was suitably fitted with the kinetic data. As shown in Figure S2 (c), the regressions of q_t versus $t^{1/2}$ were linear, but it did not pass through the origin, suggesting that the adsorption involves intraparticle diffusion but it is not the only rate-controlling step (Zhang *et al.* 2012; Wang *et al.* 2016).

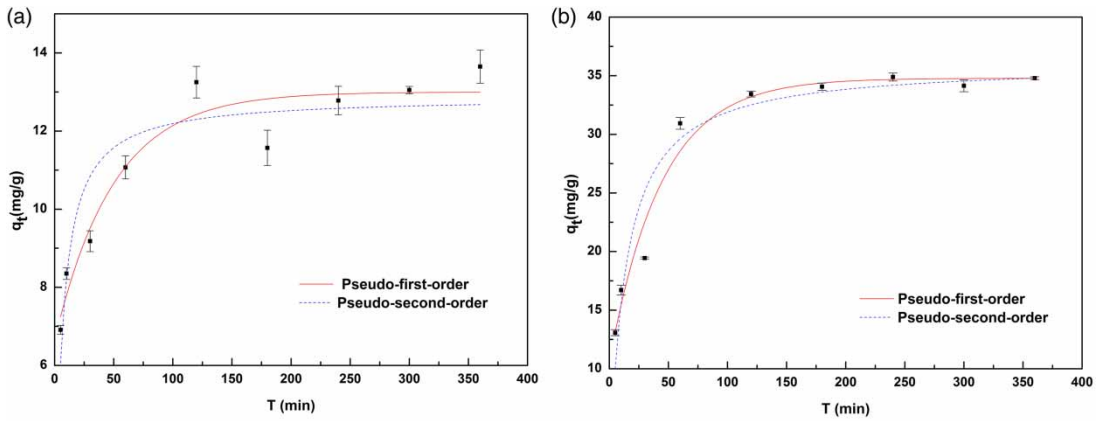

Figure 2 | Adsorption kinetic modeling of TCP on GO (a) and G (b). Solid and dotted lines represent kinetics fitted by the pseudo-first-order model and pseudo-second-order model, respectively. The error bars indicate the standard deviations ($n = 3$).

Table 1 | Kinetic parameters for the adsorption of TCP on GO and G

	Pseudo-first-order model		Pseudo-second-order model		Particle diffusion model	
Adsorbent	k_1 (min^{-1})	R^2	k_2 ($g \cdot mg^{-1} \cdot min^{-1}$)	R^2	k_i ($g \cdot mg^{-1} \cdot min^{-1/2}$)	R^2
GO	0.0097	0.8872	0.0064	0.9947	0.3590	0.8456
G	0.0286	0.9188	0.0021	0.9982	1.2872	0.8076

Adsorption isotherms and thermodynamic parameters

The adsorption isotherms of TCP on GO and G at 303, 323, and 343 K are shown in Figure 3. The Langmuir and Freundlich models were used to fit the isotherms. Results are shown in Figure 3 and Figure S3 (available online), and the regression parameters are listed in Table 2. Compared with the Freundlich model, the Langmuir model is much better able to describe the adsorption isotherms with relatively higher R^2 (Table 2), suggesting that the adsorption of TCP on GO and G is monolayer coverage (Liu *et al.* 2015b). The Langmuir maximum adsorption capacity for TCP on G ($q_m = 87.7$ mg·g^{-1}) at 303 K was found to be higher than that of GO ($q_m = 30.7$ mg·g^{-1}). Furthermore, an increase in the adsorption capacity is observed with an increase in temperature, which can be attributed to the increase in chemical interactions caused by an increased mobility of TCP towards the active sorption sites of GO and G at higher temperatures (Setshedi *et al.* 2015).

Moreover, the increase in TCP adsorption performance with increasing temperature is thermodynamically evaluated by estimating thermodynamic parameters including the change of Gibbs free energy (ΔG°, KJ·mol^{-1}), enthalpy change (ΔH°, KJ·mol^{-1}), and entropy change (ΔS°, J·mol^{-1}·K^{-1}). The parameter calculation is presented in the Supplemental Material (Equations (7)–(9), Figure S4), and the values are listed in Table S2 (available online). The positive ΔH° (8.537 KJ·mol^{-1} for GO, and 18.897 KJ·mol^{-1} for G) of the two adsorbents suggests the endothermic nature of adsorption, which is also supported by the increase in the adsorption capacity for TCP with the increase in temperature. The positive ΔS° (52.956 J·mol^{-1}·K^{-1} for GO, and 89.691 J·mol^{-1}·K^{-1} for G) shows the increased randomness at the solid/liquid interface. Meanwhile, the negative ΔG° values indicate the spontaneous process of TCP adsorption under the conditions applied. The decrease of ΔG° with the increase of temperature indicates more efficient adsorption at higher temperature.

Influences of process conditions on breakthrough curves

As G has a better adsorption capacity than GO, the adsorbent G was used to investigate dynamic adsorption performance. Breakthrough curves represent the effects of flow rate, initial concentration and column height on column performance with experimental data, and results are shown in Figure 4.

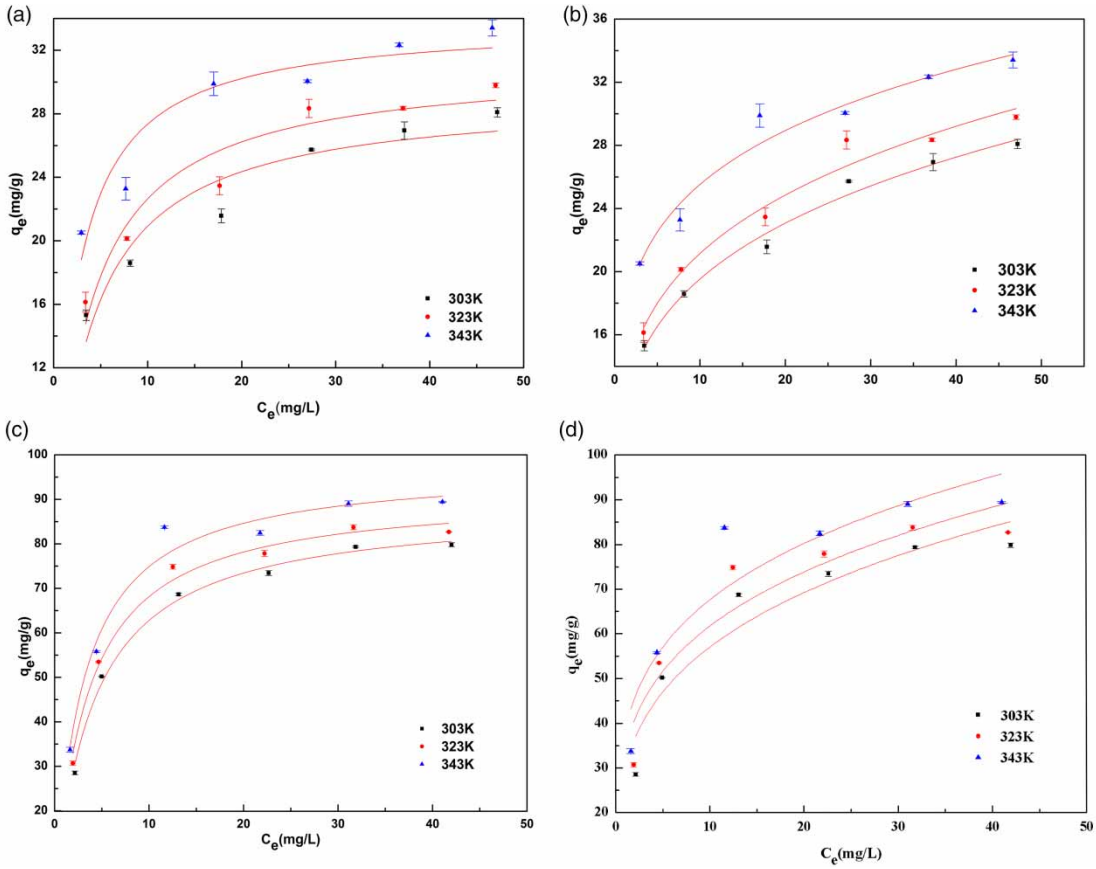

Figure 3 | Adsorption isotherms of TCP on GO (a) and (b) and G (c) and (d) at 303 K (■), 323 K (●), and 343 K (▲). Langmuir (a) and (c) and Freundlich (b) and (d) fitting for GO and G, respectively. Conditions: C_0: 5–50 mg L^{-1} of TCP solution; mass of adsorbent: 10 mg; time: 0–360 min at pH 5.

Table 2 | Parameters for Langmuir and Freundlich isotherm model

		Langmuir			Freundlich	
Adsorbent	***T***	K_L ($L \cdot mg^{-1}$)	q_m ($mg \cdot g^{-1}$)	R^2	K_F ($L^{1/n} \cdot g^{-1} \cdot mg^{1-1/n}$)	R^2
GO	303 K	0.1155	30.7	0.9790	6.0818	0.9784
	323 K	0.1029	32.3	0.9598	7.0604	0.9421
	343 K	0.1065	35.2	0.9456	8.2813	0.9211
G	303 K	0.1010	87.7	0.9886	10.9507	0.9153
	323 K	0.1297	90.1	0.9896	14.5691	0.8949
	343 K	0.1695	96.2	0.9884	19.6603	0.9145

To investigate the effect of flow rate on TCP adsorption, the flow rate varied from 3 to 10 mL·min^{-1}, while the influent TCP concentration and the column height were kept constant at 2 mg·L^{-1} and 1 cm, respectively. As shown in Figure 4(a), in the interval of 100 min, the value of C_t/C_0 reached 0.06, 0.69 and 0.83 when the flow rate was 3, 5 and 10 mL·min^{-1}, respectively. The breakthrough generally occurred earlier with higher flow rate, and breakthrough time reaching saturation was increased significantly with a decrease in the flow rate. This may be explained on the basis of mass transfer fundamentals (Ko *et al.* 2000).

The effect of feed TCP concentration on the shape of the breakthrough curves at the same flow rate (5 mL·min^{-1}) is shown in Figure 4(b). As shown in Figure 4(b), in 100 min, the value of C_t/C_0 reached 0.17, 0.70 and 0.78 when the influent concentration was 1, 2 and 3 mg·L^{-1}, respectively. It was obvious that the breakthrough time decreased with increasing influent TCP concentration. As the influent concentration increased, sharper breakthrough curves were obtained. This is because the change of concentration gradient affects the saturation rate and breakthrough time. Similar results have been reported by some other researchers (Ahmad & Hameed 2010; Zeinali *et al.* 2012).

As seen from Figure 4(c), when the height of the packing material changes, the penetration time of TCP in the aqueous solution of G and the saturation time of the adsorption all changed. When the filling height was 1, 2 and 3 cm, the breakthrough time was 30, 50 and 100 min, respectively, and the

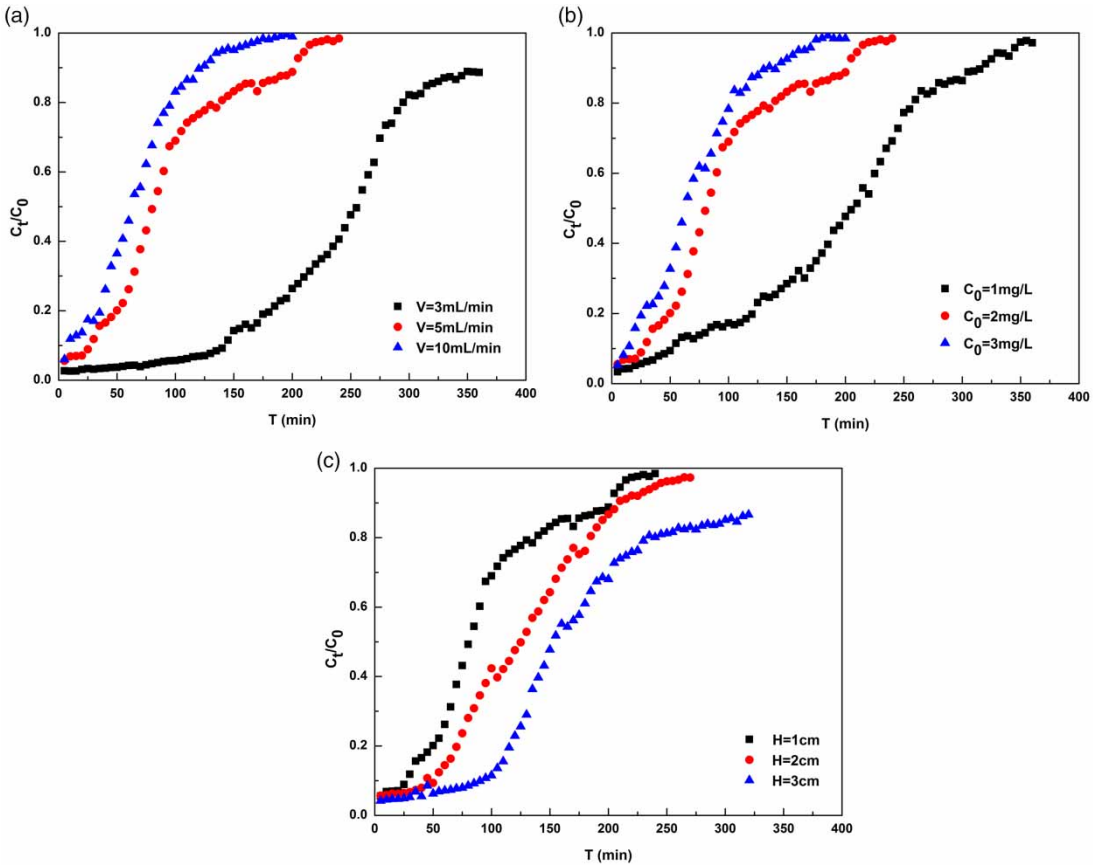

Figure 4 | (a) Influences of flow rate on TCP breakthrough on G column at 303 K ($H = 1$ cm, $C_0 = 2$ mg·L^{-1}), (b) influences of feed concentration on TCP breakthrough on G column ($H = 1$ cm, $V = 5$ mL·min^{-1}), and (c) influences of column height on TCP breakthrough on G bed ($C_0 = 2$ mg·L^{-1}, $V = 5$ mL·min^{-1}).

saturation time was 230, 290 and 330 min, respectively, showing the time of breakthrough extended with the increase in the filling height of the adsorbent. This is because that the adsorbent can make full contact with TCP and the adsorption process is more complete.

Modeling breakthrough curves

Two commonly used mathematical models, namely the Thomas and Yoon-Nelson models, are applied to fit the experimental data. The Thomas model equation in linear form can be expressed by the following equation (Chen *et al.* 2012):

$$\ln\left(\frac{C_0}{C_t} - 1\right) = \frac{k_{Th}\, q_0\, m}{Q} - k_{Th} C_0 t \tag{10}$$

where k_{Th} is the Thomas rate constant (mL·mg^{-1}·min^{-1}), m is the amount of G (g), q_0 is the saturated adsorption capacity of G (mg·g^{-1}), Q is the flow of the adsorption column (mL·min^{-1}), respectively. A linear plot of ln [(C_0/C_t) − 1] against t is used to determine the values of k_{Th} and q_0 from the slope and intercept of the plot, respectively.

The linearized Yoon-Nelson model is presented as (Yoon & Nelson 1984)

$$t = \tau + \frac{1}{k_{YN}} \ln \frac{C_t}{C_0 - C_t} \tag{11}$$

where C_t is the effluent concentration of TCP in solution (mg·L^{-1}), k_{YN} is the adsorption rate constant (min^{-1}), τ is half of the penetration time (min), and C_0 is the initial concentration of TCP (mg·L^{-1}), respectively. The values of k_{YN} and τ can be determined from the linear plot of ln [C_t/(C_0-C_t)] against t.

The two models above were employed to fit the breakthrough data of TCP, and are shown in Figures S5–S6 (available online). Fitting parameters are listed in Table 3. High correlation coefficients (R^2) were obtained for both the models, as shown in Table 3, thus showing an agreement between the experimental data and the mathematical

Table 3 | Thomas and Yoon-Nelson models' parameters for TCP adsorption on G

Parameters			Thomas model			Yoon-Nelson model		
H (cm)	C_0 (mg·L^{-1})	V (mL·min^{-1})	k_{Th} (L·mg^{-1}·min^{-1})	q_0 (mg·g^{-1})	R^2	k_{YN} (min^{-1})	τ (min)	R^2
1	2	3	0.009	34.4	0.9721	0.018	242.88	0.9717
1	2	5	0.0135	21.9	0.9564	0.027	94.46	0.9554
1	2	10	0.0188	16.2	0.9904	0.0375	65.27	0.9902
1	1	5	0.0181	26.3	0.9824	0.018	188.25	0.9821
1	2	5	0.0135	21.9	0.9564	0.027	94.46	0.9554
1	3	5	0.0127	14.8	0.9814	0.035	69.20	0.9809
1	2	5	0.0135	21.9	0.9564	0.027	94.46	0.9554
2	2	5	0.0127	13.1	0.9952	0.0254	125.39	0.9951
3	2	5	0.0094	12.5	0.9510	0.0187	180.45	0.9503

models. For both the Thomas and Yoon-Nelson models, their parameters k_{Th} and k_{YN} (Table 3) show an increasing trend, with the flow rate increasing from 3 to 10 mL·min^{-1}, which explains the result that the breakthrough and saturation occurred faster at a higher flow rate (Figure 4(a)). It was also noted that the values of k_{Th} increase while those of q_0 decrease with an increase in the influent TCP concentration for the Thomas model. The k_{YN} values show an increase with increasing influent TCP concentration due to the increased driving force of mass transfer in the liquid film (Setshedi *et al.* 2015). This explained the result that the breakthrough curves became steeper with a higher influent concentration (Figure 4(b)). In addition, for both the Thomas and Yoon-Nelson models, their parameters k_{Th} and k_{YN} (Table 3) show a decreasing trend with increasing column height (Figure 4(c)).

CONCLUSIONS

Comparative studies were performed toward kinetics and equilibrium of TCP adsorption on GO and G. The adsorption kinetics exhibited a rapid TCP uptake by GO and G, and experimental data were well described by the pseudo-second-order kinetic model. Adsorption isotherm data of TCP on G displayed an improved TCP removal performance with increasing temperature at pH 5, while experimental data were well described by the Langmuir isotherm model with a maximum adsorption capacity of 87.7 mg·g^{-1} at 303 K. The thermodynamic parameters (ΔG°, ΔS°, and ΔH°) can be calculated from the adsorption isotherms of TCP on GO and G, indicating that the adsorption reaction is a spontaneous and endothermic process. G proved to be superior to GO in terms of physical properties (e.g., specific surface area) as well as adsorption capacity and rate toward TCP. Furthermore, dynamic adsorption of TCP in a fixed G column confirmed a faster approach to breakthrough at high flow rate, high influent TCP concentration, and low filling height of adsorbent, while breakthrough data presented a good match with both the Thomas and Yoon-Nelson models. Therefore, G nanomaterials may be potential adsorption materials for TCP removal from wastewater if they are synthesized in large scale and at low price in the near future.

ACKNOWLEDGEMENTS

This research has been supported by Jiangsu Province Research Joint Innovation Fund-Prospective Joint Research Project (BY2014123-08), Yangzhou Basic Research Development Program (YZ2016004), Yangzhou Prospective Research Program (YZ2016198), and Jiangsu Collaborative Innovation Center of Technology and Material of Water Treatment.

REFERENCES

Ahmad, A. & Hameed, B. 2010 Fixed-bed adsorption of reactive azo dye onto granular activated carbon prepared from waste. *J. Hazard. Mater.* **175** (1–3), 298–303.

Al-Khateeb, L., Almotiry, S. & Salam, M. 2014 Adsorption of pharmaceutical pollutants onto graphene nanoplatelets. *Chem. Eng. J.* **248**, 191–199.

Cao, Z., Xu, F., Covaci, A., Wu, M., Wang, B., Yu, G., Wang, H., Huang, J., Deng, S. & Wang, X. 2014a Distribution patterns of brominated, chlorinated and phosphorous flame retardants

with particle size in indoor and outdoor dust and implications for human exposure. *Environ. Sci. Technol.* **48** (15), 8839–8846.

Cao, S., Zeng, X., Song, H., Li, H., Yu, Z., Sheng, G. & Fu, J. 2014b Levels and distributions of organophosphate flame retardants and plasticizers in sediment from Taihu Lake, China. *Environ. Toxicol. Chem.* **31** (7), 1478–1484.

Chen, S., Yue, Q., Gao, B., Li, Q., Xu, X. & Fu, K. 2012 Adsorption of hexavalent chromium from aqueous solution by modified corn stalk: a fixed-bed column study. *Bioresour Technol.* **113**, 114–120.

Ding, J., Shen, X., Liu, W., Covaci, A. & Yang, F. 2015 Occurrence and risk assessment of organophosphate esters in drinking water from Eastern China. *Sci. Total Environ.* **538**, 959–965.

He, C., Zheng, J., Qiao, L., Chen, S., Yang, J., Yuan, J., Yang, Z. & Mai, B. 2015 Occurrence of organophosphorus flame retardants in indoor dust in multiple microenvironments of southern China and implications for human exposure. *Chemosphere* **133**, 47–52.

Ho, Y. & McKay, G. 1998 Sorption of dye from aqueous solution by peat. *Chem. Eng. J.* **70** (2), 115–124.

Ishikawa, S., Uchimura, Y., Baba, K., Eguchi, Y. & Kido, K. 1992 Photochemical behavior of organic phosphate esters in aqueous solutions irradiated with a mercury lamp. *Bull. Environ. Contam. Toxicol.* **49** (3), 368–374.

Jin, Z., Wang, X., Sun, Y., Ai, Y. & Wang, X. 2015 Adsorption of 4-n-nonylphenol and bisphenol-A on magnetic reduced graphene oxides: a combined experimental and theoretical studies. *Environ. Sci. Technol.* **49** (15), 9168–9175.

Kim, J., Isobe, T., Chang, K., Amano, A., Maneja, R., Zamora, P., Siringan, F. & Tanabe, S. 2011 Levels and distribution of organophosphorus flame retardants and plasticizers in fishes from Manila Bay, the Philippines. *Environ. Pollut.* **159** (12), 3653–3659.

Ko, D., Porter, J. & McKay, G. 2000 Optimized correlations for the fixed bed adsorption of metal ions on bone char. *Chem. Eng. Sci.* **55** (23), 5819–5829.

Liu, J., Du, H., Yuan, S., He, W., Yan, P. & Liu, Z. 2015a Alkaline deoxygenated graphene oxide as adsorbent for cadmium ions removal from aqueous solutions. *Water Sci. Technol.* **71** (11), 1611–1619.

Liu, J., Li, P., Xiao, H., Zhang, Y., Shi, X., Lü, X. & Chen, X. 2015b Understanding flocculation mechanism of graphene oxide for organic dyes from water: experimental and molecular dynamics simulation. *AIP Adv.* **5** (12), 117151.

Lu, J., Ji, W., Ma, S., Yu, Z., Wang, Z., Li, H., Ren, G. & Fu, J. 2014 Analysis of organophosphate esters in dust, soil and sediment samples using gas chromatography coupled with mass spectrometry. *Chin. J. Anal. Chem.* **42** (6), 859–865.

Marcano, D., Kosynkin, D., Berlin, J., Siniskii, A., Sun, Z., Slesarev, A., Alemany, L., Lu, W. & Tour, J. 2010 Improved synthesis of graphene oxide. *ACS Nano.* **4** (8), 4806–4814.

Martínez-Carballo, E., González-Barreiro, C., Sitka, A., Scharf, S. & Gans, O. 2007 Determination of selected organophosphate esters in the aquatic environment of Austria. *Sci. Total Environ.* **388** (1–3), 290–299.

Regnery, J., Püttmann, W., Merz, C. & Berthold, G. 2011 Occurrence and distribution of organophosphorus flame retardants and plasticizers in anthropogenically affected groundwater. *J. Environ. Monit.* **13** (2), 347–354.

Ren, G., Chen, Z., Feng, J., Ji, W., Zhang, J., Zheng, K., Yu, Z. & Zeng, X. 2016 Organophosphate esters in total suspended particulates of an urban city in East China. *Chemosphere* **164**, 75–83.

Setshedi, K., Bhaumik, M., Onyango, M. & Maity, A. 2015 High-performance towards Cr (VI) removal using multi-active sites of polypyrrole-graphene oxide nanocomposites: batch and column studies. *Chem. Eng. J.* **262**, 921–931.

van der Veen, I. & de Boer, J. 2012 Phosphorus flame retardants: properties, production, environmental occurrence, toxicity and analysis. *Chemosphere* **88** (10), 1119–1153.

Wang, J., Chen, Z. & Chen, B. 2014 Adsorption of polycyclic aromatic hydrocarbons by graphene and graphene oxide nanosheets. *Environ. Sci. Technol.* **48** (9), 4817–4825.

Wang, J., Chen, B. & Xing, B. 2016 Wrinkles and folds of activated graphene nanosheets as fast and efficient adsorptive sites for hydrophobic organic contaminants. *Environ. Sci. Technol.* **50** (7), 3798–3808.

Wei, G., Li, D., Zhuo, M., Liao, Y., Xie, Z., Guo, T., Li, J., Zhang, S. & Liang, Z. 2015 Organophosphorus flame retardants and plasticizers: sources, occurrence, toxicity and human exposure. *Environ. Pollut.* **196** (1), 29–46.

Xu, J., Wang, L. & Zhu, Y. 2012 Decontamination of bisphenol A from aqueous solution by graphene adsorption. *Langmuir* **28** (22), 8418–8425.

Yoon, Y. & Nelson, J. 1984 Application of gas adsorption kinetics I. A theoretical model for respirator cartridge service life. *Am. Ind. Hyg. Assoc. J.* **45** (8), 509–516.

Yuan, X., Lacorte, S., Cristale, J., Dantas, R., Sans, C., Esplugas, S. & Qiang, Z. 2015 Removal of organophosphate esters from municipal secondary effluent by ozone and UV/H_2O_2 treatments. *Sep. Purif. Technol.* **156** (3), 1028–1034.

Zeinali, F., Ghoreyshi, A. & Najafpour, G. 2012 Removal of toluene and dichloromethane from aqueous phase by granular activated carbon (GAC). *Chem. Eng. Commun.* **199** (2), 203–220.

Zhang, S., Shao, T., Kose, H. & Karanfil, T. 2012 Adsorption kinetics of aromatic compounds on carbon nanotubes and activated carbons. *Environ. Toxicol. Chem.* **31** (1), 79–85.

Zhao, G., Li, J., Ren, X., Chen, C. & Wang, X. 2011a Few-layered graphene oxide nanosheets as superior sorbents for heavy metal ion pollution management. *Environ. Sci. Technol.* **45** (24), 10454–10462.

Zhao, G., Jiang, L., He, Y., Li, J., Dong, H., Wang, X. & Hu, W. 2011b Sulfonated graphene for persistent aromatic pollutant management. *Adv. Mater.* **23** (34), 3959–3963.

Zhou, Y., Apul, O. & Karanfil, T. 2015 Adsorption of halogenated aliphatic contaminants by graphene nanomaterials. *Water Res.* **79** (1), 57–67.

First received 8 March 2017; accepted in revised form 11 May 2017. Available online 15 June 2017